

pubs.acs.org/cm Article

Mapping Grains, Boundaries, and Defects in 2D Covalent Organic Framework Thin Films

Ioannina Castano,[○] Austin M. Evans,[○] Roberto dos Reis, Vinayak P. Dravid,* Nathan C. Gianneschi,* and William R. Dichtel*



Cite This: *Chem. Mater.* 2021, 33, 1341–1352



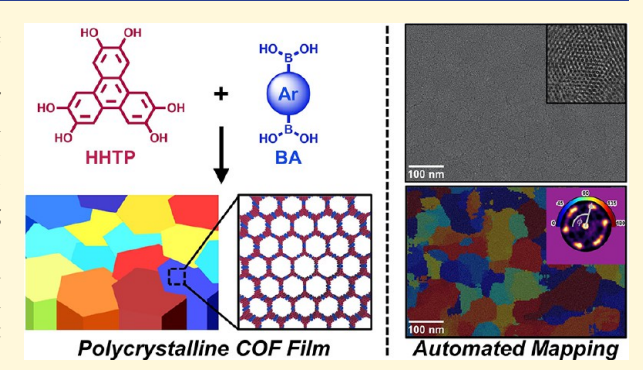
ACCESS

Metrics & More

Article Recommendations

Supporting Information

ABSTRACT: To improve their synthesis and ultimately realize the technical promise of two-dimensional covalent organic frameworks (2D COFs), it is imperative that a robust understanding of their structure be developed. However, high-resolution transmission electron microscopy (HR-TEM) imaging of such beam-sensitive materials is an outstanding characterization challenge. Here, we overcome this challenge by leveraging low electron flux imaging conditions and high-speed direct electron counting detectors to acquire high-resolution images of 2D COF films. We developed a Fourier mapping technique to rapidly extract nanoscale structural information from these TEM images. This postprocessing script analyzes the evolution of 2D Fourier transforms across a TEM image, which yields information about polycrystalline domain orientations



and enables quantification of average domain sizes. Moreover, this approach provides information about several types of defects present in a film, such as overlapping grains and various types of grain boundaries. We also find that the pre-eminent origin of defects in COF-5 films, a prototypical boronate ester-linked COF, arises as a consequence of broken B—O bonds formed during polymerization. These results suggest that the nanoscale features observed are a direct consequence of chemical phenomena. Taken together, this mapping approach provides information about the fundamental microstructure and crystallographic underpinnings of 2D COF films, which will guide the development of future 2D polymerization strategies and help realize the goal of using 2D COFs in a host of thin-film device architectures.

■ INTRODUCTION

Two-dimensional (2D) covalent organic frameworks (COFs) are synthetically versatile 2D polymers that have a unique confluence of covalent connectivity, permanent porosity, and structural precision.¹⁻⁴ This combination of properties has inspired interest in 2D COFs as catalysts, 5-7 membranes, 8-11 and active layers in organic electronic devices. 12-14 However, a major hurdle is that COFs are commonly prepared as aggregated powders, but they must be integrated into thinfilm device architectures to harness many of their desirable properties. 15,16 Many 2D COF film fabrication approaches have been investigated including interfacial polymerization, 10,17 exfoliation followed by solution casting, ^{18,19} and solvothermal growth. 20–22 Of these methods, solvothermal growth, where films are grown directly on a solid support, has proven to be an operationally simple method for growing highly crystalline and vertically oriented films.²¹ However, these films are often contaminated by insoluble powder aggregates formed during synthesis, which further complicates direct imaging.² Although conventionally prepared films have been studied extensively by bulk characterization methods, such as grazingincidence wide-angle X-ray scattering (GIWAXS), these

ensemble measurements are insensitive to nanoscale inhomogeneities that arise as a consequence of defects or domain edges. These uncharacterized domain boundaries and defects are likely to impact the performance of 2D COF thin films in electronic devices. Here, we leverage newly developed synthetic conditions for synthesizing 2D boronate ester-linked COFs as stable colloidal suspensions, ²³ which now also enable the preparation of 2D COF films that are not contaminated by precipitated bulk powders. These synthetic developments enable a new frontier in nanoscale characterization of 2D polymers because high-quality samples are a prerequisite for direct imaging of grain boundaries and defects in thin films.

Nanoscale features are routinely studied in beam-stable 2D materials, such as transition-metal dichalcogenides (TMDs) and graphene, and are known to produce exotic physical

Received: November 13, 2020 Revised: January 20, 2021 Published: February 4, 2021





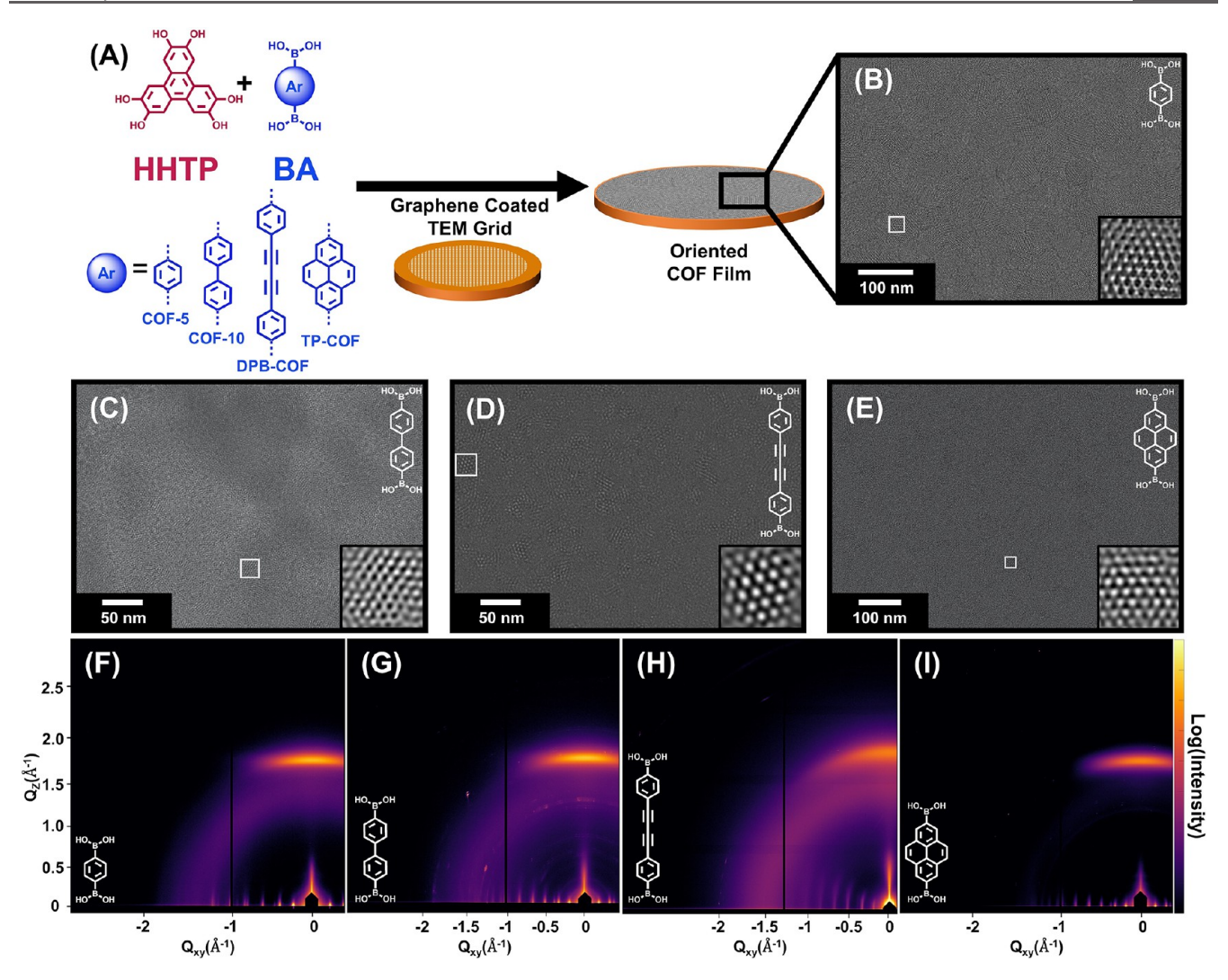


Figure 1. Preparation of 2D COF films using colloidal conditions. (A) Schematic of the synthesis of boronate ester-linked COF films on graphene-coated TEM grids. (B–E) TEM images of oriented COF films: [(B), COF-5] dose rate of 13.81 e^- Å $^{-2}$ s $^{-1}$ and cumulative dose of 13.75 e^- Å $^{-2}$; [(C), COF-10] dose rate of 17.35 e^- Å $^{-2}$ s $^{-1}$ and cumulative dose of 17.28 e^- Å $^{-2}$; [(D), DPB-COF] dose rate of 16.45 e^- Å $^{-2}$ s $^{-1}$ and cumulative dose of 6.40 e^- Å $^{-2}$; [(E), TP-COF] dose rate of 2.12 e^- Å $^{-2}$ s $^{-1}$ and cumulative dose of 0.41 e^- Å $^{-2}$. Insets: magnified image of the small boxed region in each micrograph after band pass filtering. (F–I) GIWAXS of COF films on graphene-coated SiO₂ grown concurrently with the TEM grids: (F) COF-5, (G) COF-10, (H) DPB-COF, and (I) TP-COF.

phenomena and impact macroscale device performance.^{24,25} These materials have been previously studied using techniques such as electron backscatter diffraction (EBSD) in scanning electron microscopy (SEM), dark-field transmission electron microscopy (DF-TEM), and color-coded Fourier filtering to map domains of beam-stable crystallites, as well as highresolution TEM (HR-TEM) to determine the atomic structure of grain boundaries. 4,24-27 The Fourier filtering method takes a fast Fourier transform (FFT) of the entire image and then applies Fourier masks on a certain ring with the symmetry of the crystals being considered.⁴ For example, in a hexagonal lattice, sets of six masks that are 60° apart would be applied with the angular precision determined by the user. Using this method, grain size, shape, and distribution can be mapped. However, using predefined symmetry becomes less accurate when the domains are tilted and only two, rather than six, spots are present in the FFT pattern. In this case, a given domain would be assigned to the same color as other domains with the same rotation but without tilt and those with tilt about a different crystallographic axis. Therefore, if two such domains

were next to each other, which we would expect to occur in inherently soft 2D materials, the Fourier filtering method would not be able to distinguish them. However, the use of local FFTs, which is used in our newly developed mapping technique, would allow for these two types of domains to be distinguished. Another method for mapping the grains of materials is DF-TEM, which has a large field-of-view, making it a particularly useful technique for materials with large domain sizes, such as inorganic 2D materials. However, DF-TEM is impractical for beam-sensitive materials with large lattice parameters, such as COFs, because of the limited angular precision imparted by the physical size of the objective aperture and the requirement of a high electron flux because only one reflected beam is blocked. It is also possible to use HR-TEM imaging over smaller fields-of-view, stitch the images together, and then perform Fourier filtering to map grain boundaries. However, apart from being time-consuming, the cross-correlation during image stitching may fail if neighboring frames do not contain easily recognizable features.

In addition to these techniques, electron diffraction is particularly useful for identifying crystallite orientations and generating spatially resolved maps of those orientations by tracking the evolution of the electron diffraction patterns. 24,25,28 Despite the versatility of this technique, electron diffraction requires a focused electron beam and a long acquisition time for generating adequate signal-to-noise ratios, both of which result in high electron fluxes.^{29,30} Although diffraction focuses the electron beam onto only a few spots of the material, the high flux at those spots results in significant beam damage. Electron beam damage, which affects many materials to varying extents, 31-35 has impeded the application of diffraction techniques for soft materials, including COFs, which are particularly sensitive to electron beam damage. Despite the well-known beam sensitivity of COFs, few TEM studies mention the use of low-flux imaging conditions or report the cumulative electron flux used to acquire an image.^{36,37} In most cases, TEM characterization of COFs has been limited to analysis of the morphology and arrangement of the COF mesopores or pore channels of small sample areas. 14,20,38-45 Beyond traditional real space imaging, there are some reports of using electron diffraction 46,47 or FFT 36,48 patterns to identify crystallite orientations. Furthermore, there is only a single example of using Fourier filtering of TEM images to identify grain boundaries, grain orientations, and edge dislocations of a particularly robust triphenyl triazine thiazole-linked COF.4 Beyond these limited examples, nanoscale structural characterization of COFs remains extremely challenging and is limited to frameworks composed of highly beam-stable linkages.

Here, we develop an automated postprocessing mapping technique for extracting nanoscale information directly from HR-TEM images of four beam-sensitive boronate ester-linked COF thin films. While traditional methods used to study defects and grain boundaries of graphene and TMDs rely on tracking changes in the positions of diffraction spots, our script analyzes the change in 2D Fourier transforms across an image to identify the locations, orientations, and shapes of the grains and grain boundaries of beam-sensitive materials. 2D Fourier transforms are mathematical transformations that extract the periodicity of an image. Because FFTs can be produced after imaging, we are able to study changes in crystallinity without the need for large electron fluxes or long acquisition times, which are typically required when collecting electron diffraction patterns. By combining recent TEM hardware developments, such as high-resolution direct electron counting detectors, 34,36,49-51 and our postprocessing approach, this technique provides a high-throughput method for evaluating the synthesis of beam-sensitive polycrystalline materials at the nanoscale. This approach reveals that COF-5 films have small, irregularly shaped domains with domain edges that are most commonly offset by a 12° relative rotation, which we attribute to the formation of a hemiboronate ester. By providing researchers with previously unavailable information about fundamental chemical and structural aspects of 2D polymerizations, this mapping approach will enable improved polymerization strategies for producing high-performance COFs in thin-film device architectures.

■ RESULTS AND DISCUSSION

To prepare COF thin films suitable for TEM analysis, we polymerized 2D boronate ester-linked COFs directly onto graphene-coated TEM grids (Figure 1). The four boronate

ester-linked 2D COFs studied are COF-5, COF-10, DPB-COF, and TP-COF which are synthesized by the condensation of 2,3,6,7,10,11-hexahydroxytriphenylene (HHTP) with 1,4phenylenebis(boronic acid), 4,4'-biphenylbis(boronic acid), 4.4'-diphenylbutadiynebis(boronic acid), 52 and 2,7-pyrenebis-(boronic acid), 53 respectively. For all systems, monomer solutions of HHTP (1 mM) and the corresponding boronic acid (1.5 mM) in CH₂CN/1,4-dioxane/mesitylene (80/16/4 v/v/v) were prepared. This solution was then transferred to a vial containing both a graphene-coated silicon dioxide (SiO₂) substrate, which was used for bulk characterization techniques, and a graphene-coated TEM grid. There, films were grown on two substrates under the same conditions to enable their direct comparison. The sealed vial was then heated to 70 °C for 24 h to produce a colloidal solution and a templated COF thin film on the graphene surfaces (Figure 1A). Using colloidal synthetic conditions, no precipitates were formed, which facilitated the direct imaging of these 2D COF thin films.

Bulk characterization of the COF films indicated that the colloidal growth conditions produced highly crystalline, oriented thin films on graphene/SiO2 substrates. GIWAXS revealed that the COF films were highly crystalline and oriented on the graphene-coated SiO₂ substrates (Figure 1F-I). In all cases, the scattered intensities of the Bragg peaks were concentrated near $Q_z = 0$, which is indicative of an oriented 2D layered material. Extrapolated 1D diffraction patterns $(Q_z = 0)$ displayed sharp in-line Bragg diffraction peaks that are consistent with simulated patterns for each COF with (100) peaks at 0.24, 0.20, 0.16, and 0.19 Å⁻¹ for COF-5 (Figure 1F), COF-10 (Figure 1G), DPB-COF (Figure 1H), and TP-COF (Figure 1I), respectively. To provide an estimate of the orientational order, or mosaicity, of the film we analyzed the radial width of the (001) peaks, which appear as diffuse arcs centered around $Q_z = 1.85 \text{ Å}^{-1}$. This analysis indicates that in the COF-5 film, most grains are oriented within 11° of the surface normal (Figure S29), which is improved compared to previous COF-5 films grown under other conditions. ²¹ We also subjected the other boronate ester-linked 2D COF films to this analysis and found they are also highly oriented with most grains oriented within 10° for COF-10, 14° for DPB-COF, and 11° for TP-COF (Figures S30-S32). Additionally, Scherrer analysis of the GIWAXS patterns suggested an average crystalline domain size of 50 nm for COF-5. However, this analysis only gives an average value rather than a distribution of sizes, is limited to nanoscale crystallites (<200 nm), and fails to account for other peak-broadening factors such as dislocations, stacking faults, and grain boundaries. Therefore, while GIWAXS measurements suggest that these films are highly crystalline and oriented, this data fails to provide nanoscale information regarding how the COF crystalline domains are stitched together at the atomic level to form grains and grain boundaries.

Next, we used TEM to elucidate the nanoscale structure of the four COF thin films. To accommodate the beam sensitivity of COF materials, we used low-flux imaging conditions on a transmission electron microscope equipped with a direct electron counting detector, which enabled the acquisition of high-resolution images using short acquisition times and low electron fluxes. In all cases, the films spanned the holes of the TEM grid, as confirmed by low-resolution TEM, and were polycrystalline with domains of varying size, shape, and crystallite orientation (Figures 1B–E and S5–S9). In particular, the COF-5 film displayed excellent surface coverage

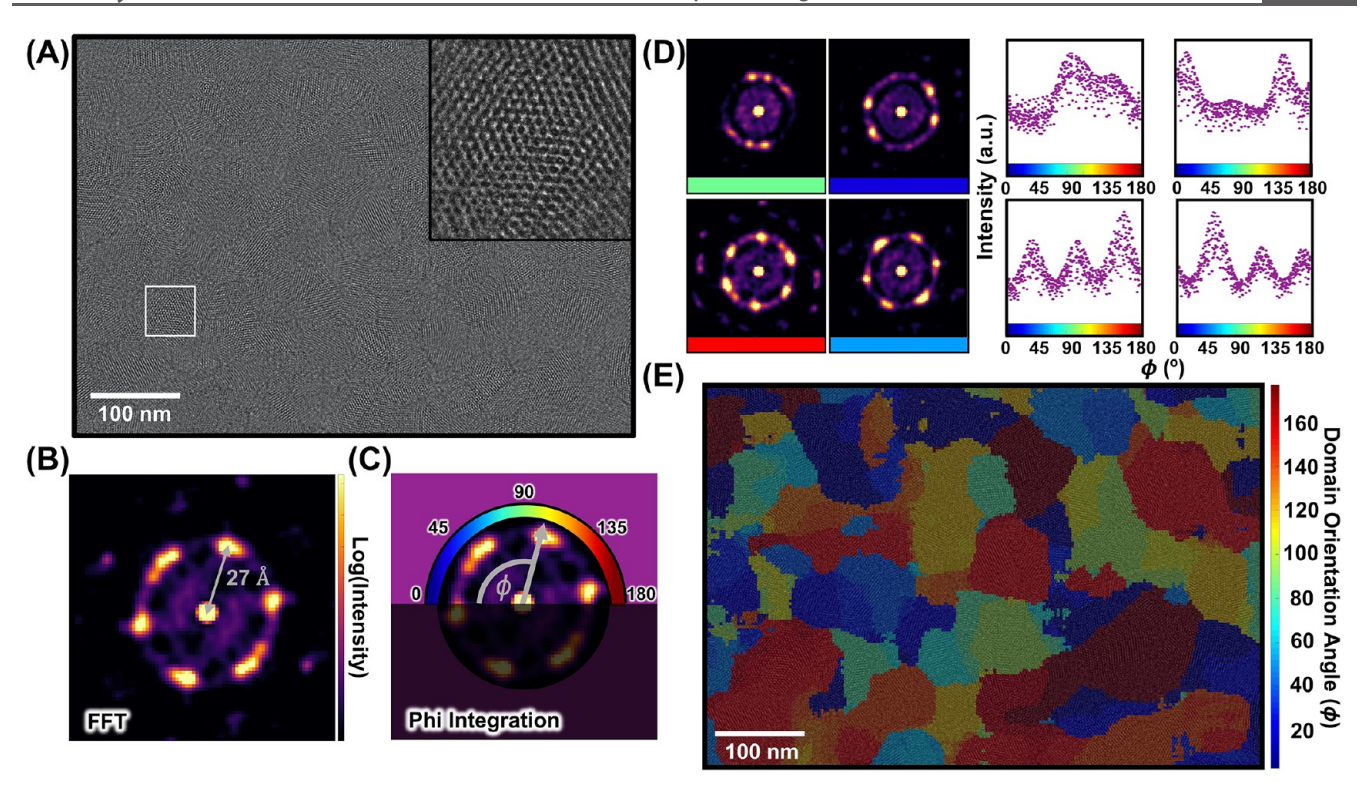


Figure 2. Schematic of automated domain mapping procedure. (A) COF-5 HR-TEM image taken with a cumulative dose of $14 e^- Å^{-2}$. Inset: magnified image of boxed region in (A) displaying polycrystalline COF-5 lattice fringes. (B) FFTs are generated by sweeping a ROI across the image. (C) A band pass filter is then applied to each FFT and a radial phi (φ) integration is applied to identify the locations of the highest intensity. (D) FFT patterns are then analyzed to locate the maximum intensity spot and the corresponding phi angle, which corresponds to a different color. The colors corresponding to the phi angles measured for each FFT are shown in the colored bar below the FFT patterns. (E) Image is then mapped using the colors corresponding to the different phi angles and overlaid on the initial TEM image.

and maintained its crystallinity over large portions (>10 μ m) of the grid, as evidenced by TEM (Figures S2–S4). While COF films can be imaged with standard CCD-based cameras, the high sensitivity of electron counting camera enables more reliable imaging of these thin, beam-sensitive materials. These qualitative observations led us to realize that the quality of these materials could enable the extraction of reliable quantitative information, which would require the development of new image analysis tools.

With this in mind, we developed a method to extract quantifiable nanoscale information such as domain size, shape, and grain boundary prevalence from TEM images using an automated postprocessing Fourier-mapping approach (Figure 2). First, we import a lattice-resolution TEM image of a polycrystalline film (Figure 2A). Next, the TEM image is subjected to a 2D fast Fourier transform (FFT) that is radially integrated in Qxy space to find the predominant repeat spacing in the image⁵⁴ (Figure 2B). The program then uses this fullimage FFT and partial-image FFT as training data to optimize radial sensitivity, mapping script accuracy, and signal-to-noise as a function of a region of interest (ROI) size, which determines the size of the box that will be scanned across the entire image to yield the most informative map (Figures S10-S13, see Supporting Information for a detailed description of selecting these parameters). After analysis, we determined that a ROI square with side lengths of around 20 crystallographic cells is optimal for mapping. For example, for COF-5 films, we used a ROI of 500 pixels (55 nm), which is small enough to capture a single domain in a frame but large enough to provide adequate signal for mapping. Next, we determine how much

the ROIs will overlap as they are rastered across the image, which effectively determines the accuracy of the resultant maps. After testing several different values, we determined that a mapping accuracy value slightly greater than the expected (100) spacing of the COF provides a well-resolved domain map without adding unnecessary computational burden (Figures S14–S17). For example, for COF-5 films, which have a (100) spacing of 2.8 nm, we selected a mapping accuracy of 3 nm.

FFT patterns obtained at appropriate spacing over large-area micrographs differentiate the orientations of adjacent crystalline domains. A Fourier transform mathematically decomposes a function into a continuous spectrum of its frequency components. Therefore, periodic structures, or lattice fringes, in a real-space TEM image can be transformed into an inversespace FFT pattern with sharp, symmetric spots, where the direction of the spots reflects the orientation of the crystallite. The FFT of a perfectly oriented boronate ester-linked COF film with hexagonal pores lying head-on would have six spots of equal intensity that are 60° apart (Figure 2A,B). In practice, however, crystallites can lie on the substrate in random orientations. Therefore, a slightly tilted hexagonal net results in a FFT pattern with projected symmetries that depict the preferential grain tilt and rotation directions (e.g., two-spots, rather than six) (Figures 2D and S19). The symmetry and intensity of these spots are highly sensitive to slight changes in the film, including thickness variations of the COF or minor height differences from the substrate. Given that FFT patterns are produced via a mathematical transformation of the image,

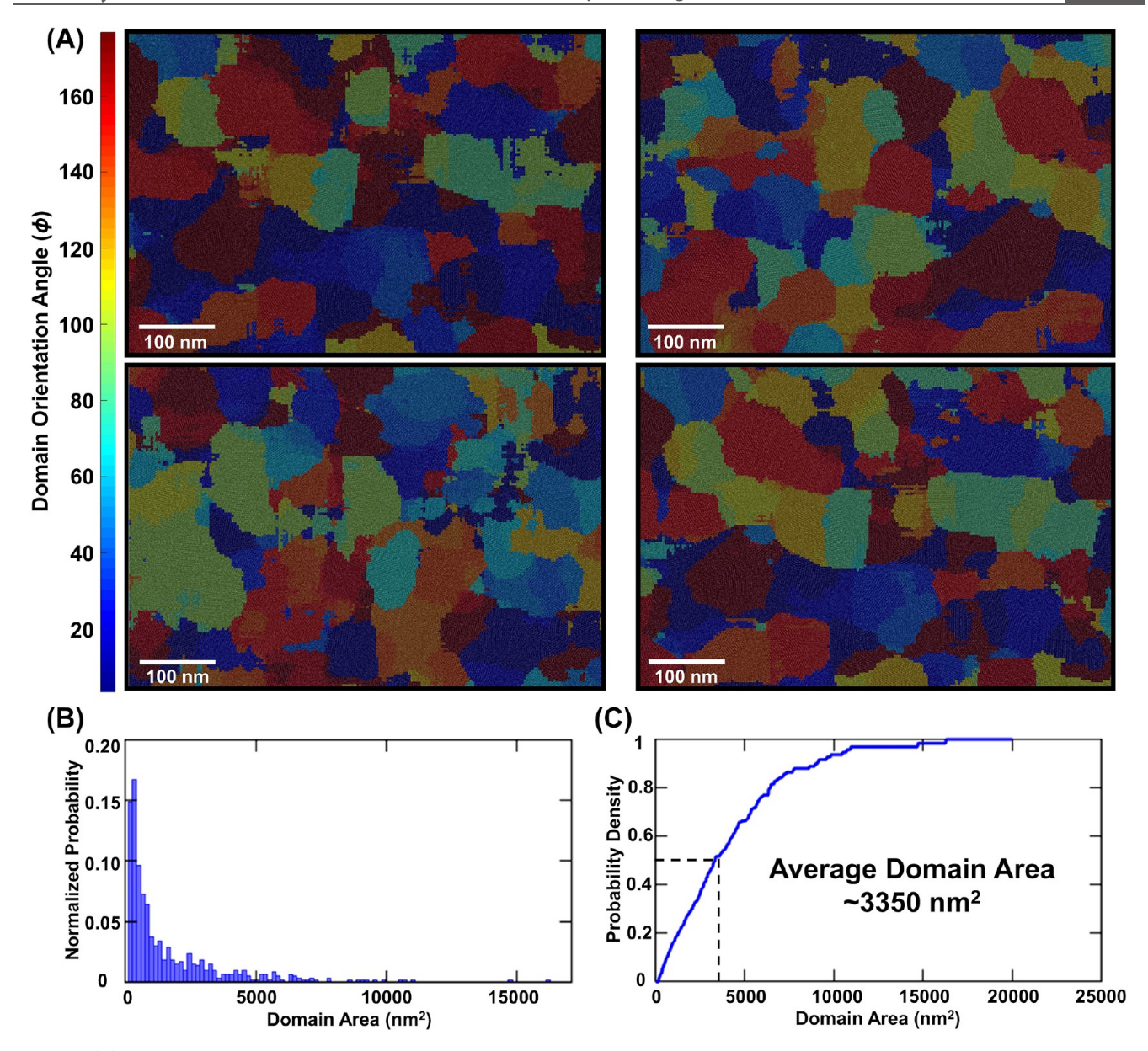


Figure 3. (A) Four COF-5 film TEM images taken from the same TEM grid with the same magnification and a cumulative dose per image of \sim 14 e⁻ Å⁻² for each image. (B) Histogram of domain areas compiled from the images in (A). (C) Probability density plot showing the likelihood of a film having a domain of a certain area with the dotted lines highlighting the average domain area expected.

they represent a convenient and powerful tool for studying the crystallinity of beam sensitive materials.

With these resultant FFT patterns from a variety of grain configurations and the appropriate selection of mapping parameters, we can then proceed to map the TEM images by rastering the ROI across the image, generating 2D FFTs at each location, and azimuthally integrating the FFT intensity to determine the phi (Φ) position of the most intense spot (Figure 2B). Using the repeat spacing determined from the full image, each FFT is band pass-filtered to focus our analysis to the spacing associated with the predominant crystallographic axis (Figure 2C). For each ROI, the script locates the FFT spot with the maximum intensity and measures the corresponding phi degree (Figure 2D) in order to identify the size, location, and orientation of each domain. If the phi degree of the maximum intensity spot in a given FFT differs by a value greater than the phi degree binning value compared to the surrounding FFTs, that corresponds to a new domain in the

image (Figure S18). We selected a phi binning value, or tolerance level, of 5° because of the inherent flexibility of 2D polymers, which results in slight bending of the lattice fringes within a single crystalline domain. Different colors are then assigned to each crystalline domain orientation, as defined by the phi angle measured in each FFT, resulting in a color-coded crystal-orientation domain map (Figures 2D,E and S19). In this work, we focus our attention on four beam-sensitive boronate ester-linked COF films (Figures S25–S27); however, this strategy can be used to map TEM images of any polycrystalline material (Figure S28).

By analyzing the statistical distribution of grain sizes in a given COF-5 film across four TEM images, we observed irregularly shaped domains with small average crystallite sizes (Figure 3). First, we took lattice-resolution TEM images of several different regions in a single COF-5 film (Figure 3A). We then subjected those images to the automated domain orientation mapping script using the parameters previously

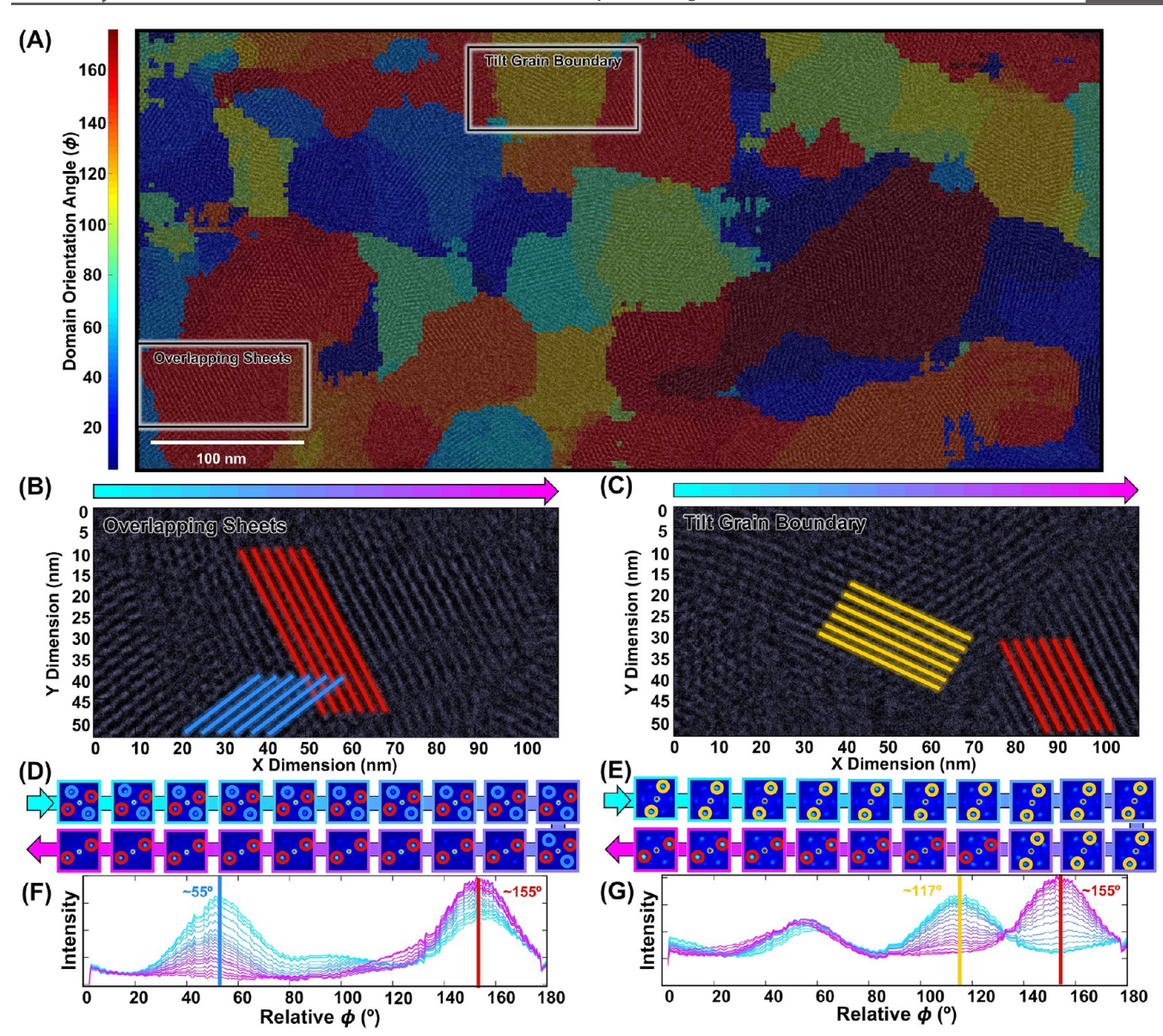


Figure 4. Analysis of COF-5 grain boundaries. (A) Domain-mapped HR-TEM image of COF-5 film. Boxed regions display different kinds of domains and grain boundaries observed in the image. Two types of grain boundaries are observed: (B,D,F) overlapping sheets and (C,E,G) tilt grain boundary. (B,C) Zoomed-in regions of COF-5 film HR-TEM image with colored lines overlaid corresponding to the phi angles of the crystalline domain orientations observed: (B) blue and red lines correspond to domain orientations of 55 and 155°, respectively; (C) yellow and red lines correspond to domain orientations of 117 and 155°, respectively. (D,E) FFT patterns of regions moving from left to right (cyan to magenta) in the cropped images shown in (B,C): (D) overlapping sheets are apparent based on the coexistence of the two sets of FFT spots in the patterns; (E) A tilt grain boundary is observed based on the simultaneous disappearance of the 117° domain (yellow) and appearance of the 155° domain (red). (F,G) Plots displaying the relative phi intensities moving from left to right (cyan to magenta) in the cropped images, which show the changes in the grain orientations.

described (Figure 2). Once the images were mapped, we used the script to extract the size of the individual domains (Figure 3A). The histogram in Figure 3B displays the grain sizes observed in the four COF-5 film images, showing that most domains are relatively small. This distribution is best evaluated by plotting the probability density, which represents the likelihood of finding a domain of a given size in a film (Figure 3C). The average domain area in a COF-5 film is 3350 nm², which corresponds to a square grain with sides that are approximately 58 nm in length. In addition to gathering statistical grain size information, this analysis also provides a method for generally evaluating the shapes of the crystalline domains. All of the COF-5 film images displayed irregularly

shaped domains and relatively small crystallites lying on the graphene substrate in several different orientations (Figure 3A). This same observation was made when studying the mapped images of other boronate ester-linked films, suggesting that whatever impedes the growth of domains in our model COF-5 system is also operative in other boronate ester-linked COFs (Figures S25–S27). We hypothesize that the irregular shapes observed are likely due to uncontrolled nucleation and growth mechanisms and therefore expect that higher quality materials can be generated if these parameters can be better controlled.

In addition to identifying grain size and orientation, this automated mapping strategy also reveals nanoscale features of

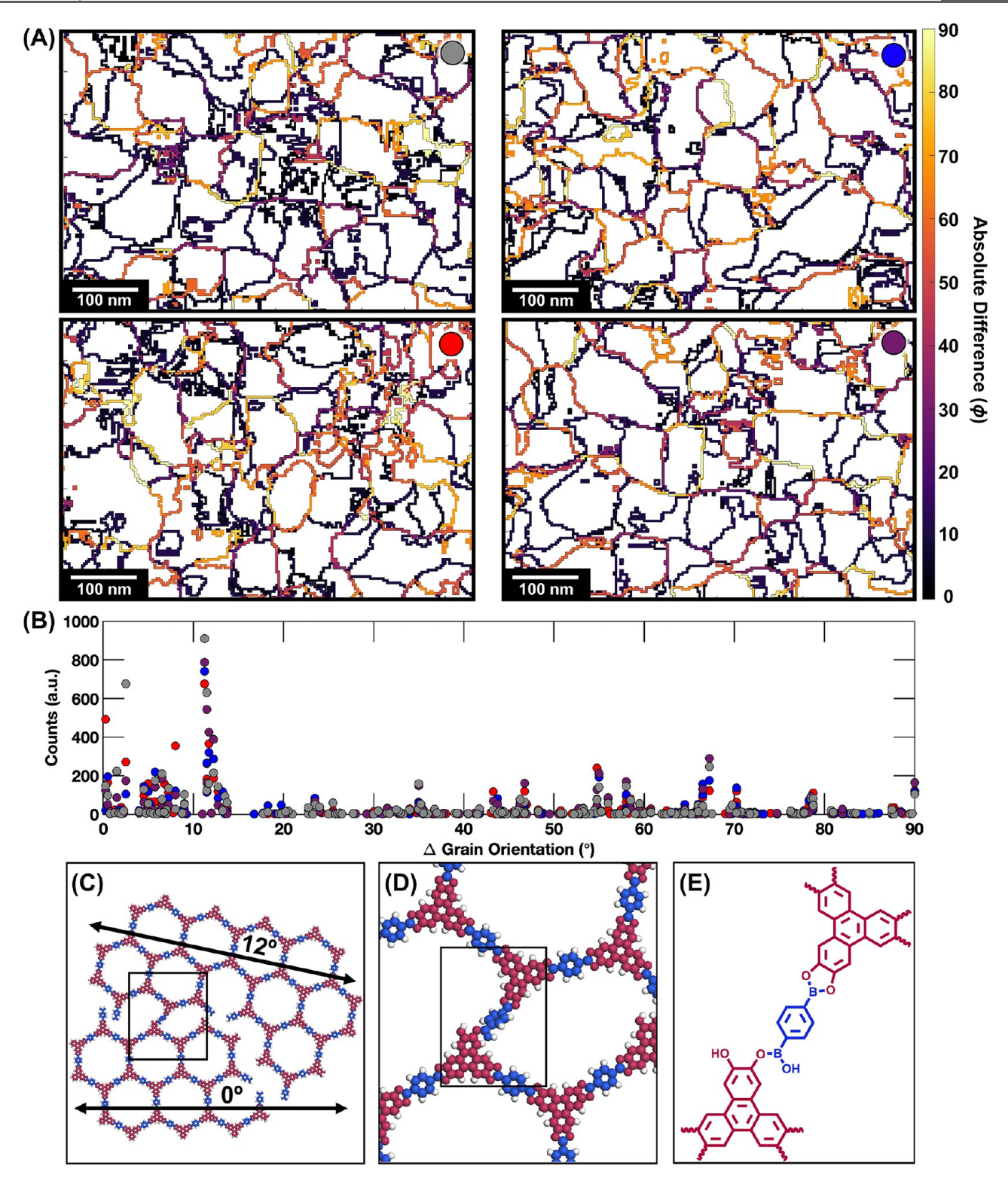


Figure 5. Statistical analysis of grain orientation. (A) Grain boundary maps of four COF-5 film TEM images taken from the same TEM grid with the same magnification and a cumulative dose per image of $\sim 14~e^-$ Å $^{-2}$ for each image. (B) Scatter plot showing the relative change in grain orientation angle measured for every grain boundary shown in (A), where the color of the dot corresponds to a particular image as shown in the top right corner of the images in (A). (C) Geometry optimized structured generated using a universal force field displaying a $\sim 12^{\circ}$ change in grain orientation between two domains. (D) Magnified image of the boxed region in (C). (E) Schematic of boxed region in (D) showing the broken B–O bond that causes the formation of a grain boundary.

crystalline films such as overlapping sheets and tilt grain boundaries by analyzing the change in phi angle and intensity of the FFT spots across the mapped image (Figure 4). In the map shown in Figure 4A, each color represents a distinct domain orientation, meaning that at the interface of one color with another, a domain boundary is present. When analyzing the changes in FFTs across boundaries, we observed two primary features: overlapping sheets and tilt grain boundaries

(Figure 4A). We identified these features by selecting regions in the mapped image that showed a visible transition from one color, or domain orientation, to another (Figure 4B,C). We then took those cropped regions and scanned a ROI box across the area, generating band pass-filtered FFTs as the ROI box moved from left to right (cyan to magenta) and radially integrating the intensities (Figure 4D,E). To identify the type of transition, we looked at the intensity variation of the FFT spots as we moved across the cropped region, which has been previously used to analyze defects in other 2D materials (Figure 4F,G).²⁴ In Figure 4F, we observe that the intensity of the FFT spots at 155° remains constant throughout the cropped region, as shown by the spots marked in red in the FFTs (Figure 4D). However, the FFT spots at 55° which are marked in blue (Figure 4D) consistently decrease in intensity as we move the ROI from left to right (cyan to magenta). This suggests that on the left side of the cropped region, we have both domains present but as we move across the image, only the 155° domain orientation remains. Because the integrated intensity is not constant over the transition, it indicates that the transition observed is due to a local overlapping of two misoriented COF domains. This is in contrast to what we observe in Figure 4G, where the intensity sum remains constant as we move from the domain with a lattice orientation of 117°, marked in yellow in the FFTs, to a domain with a lattice orientation of 155°, marked in red in the FFTs (Figure 4E), which is indicative of a tilt grain boundary without any overlapping regions. In addition to the FFT spots at 117° and 155° in the cropped region, we also observe a third set of spots at 57° that has a constant intensity throughout the image, suggesting that there is a crystalline domain with a different orientation lying outside of the focal plane. In addition to observing overlapping sheets and tilt grain boundaries, we can also use this method to analyze domains that have folds or bends as well as defect-free regions (Figures S20-S23). While other types of defects and edge dislocations are possible in COF films, such as the presence of aperiodic lines of heptagons and pentagons at interfaces,⁴ these other topological defects were not detected during our analysis of the COF grain boundaries.

Statistical analysis of the COF-5 grain boundaries and defects over several TEM images reveals that the most common change in grain orientation between two adjacent domains is approximately 12° (Figure 5). To study the grain boundaries of the films, we measure the change in domain orientation as the ROI moves from one domain, or color, on the map to the next (Figure 5A). Because each 2D FFT pattern is by definition bilaterally symmetric, we measure domain orientations from 0 to 180°. By the same logic, the absolute difference between two domain orientations is constrained from 0 to 90° (Figure S24). Through statistical analysis of COF-5 film HR-TEM images (Figure 3A), we observe that the most common change in grain orientation between adjacent domains is 12°, which is shown as a deep purple color on the grain boundary maps (Figure 5B). Considering fundamental organic bonding angles, we suspected that this 12° offset between adjacent domains could be attributed to the difference between an sp³ (109.5°) and sp² (120°) site. Chemically, we understood that this bonding difference could result as a consequence of a hemiboronate-ester defect, where only half of the functionality of a catechol condenses with a boronic acid (Figure 5E) because this would result in adjacent sp³ and sp² sites. To evaluate this hypothesis more quantitatively, we constructed a monolayer supercell of a COF-5 crystallite with an embedded broken B-O bond point defect. We then performed a geometry optimization routine to reduce stresses that originate as a function of that defect. We find that a broken B-O bond results in a 12° rotational difference between the orientation of the two simulated crystalline domains (Figure 5D,E), consistent with our experimental imaging analysis. At this stage, our assignment of this bond defect is a hypothesis that is consistent with the predominant 12° rotational offset between grains and the known chemistry of boronate esters. While this type of bonding defect is a plausible explanation, further analysis is required to unambiguously characterize the defects present at boronate ester-linked 2D COF grain boundaries. Furthermore, we find that as the simulated structure relaxes, random nonfaceted domain edges are produced. Experimentally, we also find that domain edges between COF crystallites are highly random. This is in contrast to materials such as graphene that are known to have distorted pentagons and heptagons at domain interfaces. 24,25 This observation suggests that as COF layers are polymerized on the surface, molecular bonding defects are introduced into the layers that lead to mesoscale domain boundaries. Presumably, if these defects could be more efficiently annealed out of the final structure, larger crystalline domain sizes could be obtained.

CONCLUSIONS

The combination of an improved method for preparing uncontaminated 2D COF films and HR-TEM images taken using low electron flux conditions and high-speed direct electron counting detectors revealed the overall polycrystalline structure of these emerging materials and provided insights into their grain boundaries and defects. An automated postprocessing Fourier mapping technique applied to the TEM images rapidly extracted these nanoscale features, which are otherwise difficult to obtain for beam-sensitive 2D boronate ester-linked COF thin films. Using this method, we identified the locations, orientations, and shapes of crystalline domains by relying on the information provided by FFT patterns across a TEM image. We also extracted quantitative information such as distributions of domain size and studied nanoscale features such as point defects and grain boundaries. By applying this method to a COF-5 film, we observed irregularly shaped domains with small average crystallite sizes of approximately 3350 nm². Additionally, analysis of domain interfaces revealed regions with overlapping sheets and tilt grain boundaries, where the most common difference in grain orientation between two adjacent domains was 12°. We attribute this 12° difference to a hemiboronate ester bonding defect that occurs during the polymerization and leads to mesoscale domain boundaries, highlighting that the observations enabled by this approach have real chemical consequences and provide previously unavailable information about fundamental aspects of 2D polymerizations. We anticipate that the nanoscale information provided by this method will guide the development of 2D COF thin film polymerization strategies to produce higher-quality materials, which is a necessary step toward their use in a host of thin-film device architectures.

■ MATERIALS AND METHODS

Materials. 2,7-Pyrenebis(boronic acid)⁵³ and 4,4′-diphenylbutadiynebis(boronic acid)⁵² were prepared according to

literature conditions. NMR data is consistent with those previously reported. Reagents were purchased in reagent grade from commercial suppliers and used without further purification, unless otherwise described. Solvents were obtained from commercial sources and used without further purification. PELCO Single Layer Graphene TEM Support Films on Lacey Carbon, 300 Mesh Copper Grids (Ted Pella, Redding, CA) were used for all TEM experiments. The thickness for a single layer of graphene is approximately 0.35 nm with a transparency on the order of 96.4%. Monolayer graphene SiO $_2$ /Si (10 mm × 10 mm) substrates (University Wafer) were used for all GI-WAXS and AFM experiments.

Instrumentations and Characterizations. Optical images of the TEM grids were obtained using a trinocular biological compound microscope (T490B-PL, AmScope) equipped with an 18 MP camera. Grazing-incidence wide-angle X-ray scattering (GI-WAXS) measurements were performed at Sector 8-ID-E (beam energy = 10.92 keV) of the Advanced Photon Source at Argonne National Laboratory. Samples were placed under vacuum and aligned to provide an incident angle of ~0.14°. Frames were collected for an amount of time such that the maximum pixel intensity did not exceed 80%. Diffraction patterns were collected using a Pilatus 2D detector. All radially integrated patterns were found to agree with previously reported diffraction patterns. Atomic force microscopy (AFM) images were collected using a Bruker Dimension Fastscan AFM in tapping mode. TEM was performed using a JEOL (JEOL USA, Inc., Peabody, MA) ARM300F GrandARM TEM operating at 300 keV equipped with a Gatan (Gatan, Inc., Pleasanton, CA) K3-IS "direct electron" detector (FEG emission: 15 μ A, spot size 5, 150 μ m CL aperture). The ARM300F was aligned for low-dose imaging, measuring the dose rate on the K3 detector through vacuum (no grid inserted). The dose rate was measured to be $2.1-19.6 \text{ e}^{-} \text{ Å}^{-2} \text{ s}^{-1} (5760 \times 4092 \text{ pixels})$ with image exposure times of 0.2-1 s (0.4-19.5 e⁻ Å⁻² cumulative dose per image). A JEOL (JEOL USA, Inc., Peabody, MA) ARM200CF Aberration-Corrected STEM/TEM operated at 200 keV equipped with a Gatan (Gatan, Inc., Pleasanton, CA) K2 "direct electron" detector (FEG Emission: 5 μ A, spot size 3, 150 μ m CL aperture) was used for Figures S2 and S3. The ARM200CF was aligned for low-dose imaging, measuring the dose rate on the K2 detector through vacuum (no grid inserted). The dose rate was measured to be 3.0–3.7 e $^{-}$ Å $^{-2}$ s $^{-1}$ (3710 \times 3838 pixels) with image exposure times of 1 s (3.0–3.6 e⁻ Å⁻² cumulative dose per image). All image acquisition was done using the Gatan Microscopy Suite (GMS), Digital Micrograph (Gatan, Inc., Pleasanton, CA).

Synthesis of Colloidal COF Films and TEM Sample Preparation. 2,3,6,7,10,11-Hexahydroxytriphenylene (HHTP, 1 mM) and the appropriate corresponding boronic acid (BA, 1.5 mM) were dissolved in a mixture of CH₃CN/1,4-dioxane/mesitylene (80/16/4 v/v/v; 20 mL) and sonicated for 5 min. The solution was passed through Fisherbrand qualitative-grade plain filter paper (diameter: 5.5 cm, P4 grade) via vacuum filtration to remove insoluble particulates.

All COF films (COF-5, TP-COF, DPB-COF, and COF-10) were prepared via solvothermal growth. For each system, 20 mL of monomer solution was placed in a 20 mL scintillation vial. A PELCO single-layer graphene (lacey-carbon, Cu, 300 mesh) TEM grid (Ted Pella, Redding, CA) and a 10 mm \times 10 mm monolayer graphene SiO₂/Si substrate (University Wafer) was placed in each vial. The vials were sealed and heated on a hot plate at 70 °C without stirring for 24 h, which resulted in stable, colloidal suspensions.

The colloidal solutions were then decanted from the vials and the TEM grid and substrate were retrieved using tweezers. The TEM grids were immediately rinsed with fresh $CH_3CN/1,4$ -dioxane/ mesitylene (80/16/4 v/v/v; 20 mL) solvent and allowed to dry open to air. The TEM grids were then stored in a standard grid box inside of a desiccator prior to imaging.

Mapping Script Information. Scripts were written using MATLAB version 2019b. Image and Metadata importing was done using a modified version of a file publicly available on MATLAB's Central File Exchange.⁵

The user first selects a region of interest (ROI) size in pixels, known as the pixel frame. This number is the side of a square in pixels. A smaller ROI has advantages in terms of accuracy and amount of data, while a larger ROI has improved signal to noise. For this work, we selected a ROI size that houses at least 20 repeat units. Next, a spatial accuracy is selected, corresponding to the size of the square in the final mapped image. The accuracy determines how much the ROIs overlap as they raster across the image. The entire image is then subjected to a two-dimensional (2D) Fourier-transform, which is then integrated in Q_{xy} space to find the location of the primary repeat spacing in the image. This is then transformed to a real space number, which is used to determine appropriate band pass filtering in later steps. Alternatively, the user can specify the repeat unit spacing in real space, if that spacing is known a priori. Next, the ROI is scanned across the entire image, generating FFTs at each ROI and radially integrating the intensities (phi integration). The location of the maximum intensity spot in each FFT and corresponding phi degree are then extracted. If the phi degree of the maximum intensity spot in the FFT differs by greater than the phi degree binning number (imposed by the user in the script), that corresponds to a new domain in the image. Each color in the domain orientation map corresponds to a specific lattice orientation as defined by the phi angle measured from the FFTs.

The identification of the brightest spot of a region of interest's (ROI) FFT was accomplished by the following workflow. (1) First, the FFT was masked (five pixel circle mask) to block intensities of the center spot (i.e., these intensities were reduced to zero). (2) The masked FFT was band pass-filtered to select for the FFT intensity related to the 100 feature (i.e., spacings related to the 100 spacing ± 5 Å). (3) Because of the two-fold symmetry of FFT patterns, we then summed each half of the radial intensities (i.e., $0-180^{\circ}$ and $180-360^{\circ}$, taking into account the rotational offset). (4) This intensity was then radially integrated to produce a 1D plot of intensity vs the phi angle from 0 to 180° . (5) The maximum intensity was then identified from this plot.

Unless otherwise noted, the mapping script accuracy, pixel frame, and phi degree binning used to map the images in this manuscript were 3 nm, 500 pixel frames, and 5° , respectively. All scripts are available on GitHub.

Geometry Optimization. Simulations of molecular defects in 2D COF monolayers were carried out in Materials Studio (ver.5.0).3 First, the unit cell was constructed piecewise in a highly symmetric P6/mmm unit cell with the a = b lattice parameter approximately set to be the distance between two COF vertices. The c parameter was set to be 3.5 Å, which is the interlayer spacing of graphene. We then used a Forcite geometry optimization routine with a universal force field to optimize the unit cell size with convergence tolerances of energy = 10^{-3} kcal mol⁻¹ and force = 0.5 kcal mol⁻¹ Å⁻¹. This routine produced the COF-5 unit cell we have observed in previous reports.⁴ We then created a supercell monolayer of this structure (Figure 5C). Next, we removed all crystallographic constraints to produce a largearea COF-5 sheet. Then, we selected an unreacted boronic acid at the edge of a COF crystal and installed a hemiboronate ester at that position. From that position, we constructed a second pristine COF sheet from that defect site of approximately the same size as the first. Once a crude version of the defective COF sheet was produced, we then conducted a geometry optimization routine using Forcite with the convergence tolerances of 10⁻⁵ kcal mol⁻¹ and 10⁻³ kcal mol⁻¹ $Å^{-1}$ and displacement of 10^{-5} Å. This produced the structure observed in Figure 5C,D that showed a 12-degree offset between domains. Importantly, each individual COF domain, outside of the defective boundary, relaxed nicely to the expected COF structure.

ASSOCIATED CONTENT

Supporting Information

The Supporting Information is available free of charge at https://pubs.acs.org/doi/10.1021/acs.chemmater.0c04382.

Optical images of the graphene-coated TEM grids, additional TEM images of the COF films, information

regarding selection of a ROI/pixel frame, mapping script accuracy, phi degree binning, and other domain mapping parameters when using the MATLAB script, analysis of COF-5 grain boundaries, additional domain maps of other boronate ester-linked COFs, domain mapping of other materials, and GIWAXS spectra of the COF films (PDF)

AUTHOR INFORMATION

Corresponding Authors

Vinayak P. Dravid — Department of Materials Science and Engineering, Northwestern University Atomic and Nanoscale Characterization Center, and International Institute for Nanotechnology, Northwestern University, Evanston, Illinois 60208, United States; orcid.org/0000-0002-6007-3063; Email: v-dravid@northwestern.edu

Nathan C. Gianneschi — Department of Chemistry,
Northwestern University, Evanston, Illinois 60208, United
States; Department of Materials Science and Engineering,
International Institute for Nanotechnology, Department of
Biomedical Engineering, Department of Pharmacology,
Simpson Querrey Institute, and Chemistry of Life Processes
Institute, Northwestern University, Evanston, Illinois 60208,
United States; Occid.org/0000-0001-9945-5475;
Email: nathan.gianneschi@northwestern.edu

William R. Dichtel — Department of Chemistry, Northwestern University, Evanston, Illinois 60208, United States; orcid.org/0000-0002-3635-6119; Email: wdichtel@northwestern.edu

Authors

Ioannina Castano – Department of Chemistry, Northwestern University, Evanston, Illinois 60208, United States; orcid.org/0000-0001-6491-2170

Austin M. Evans — Department of Chemistry, Northwestern University, Evanston, Illinois 60208, United States;
ocid.org/0000-0002-3597-2454

Roberto dos Reis — Department of Materials Science and Engineering, Northwestern University, Evanston, Illinois 60208, United States

Complete contact information is available at: https://pubs.acs.org/10.1021/acs.chemmater.0c04382

Author Contributions

^OI.C. and A.M.E. contributed equally to this work. The manuscript was written with contributions from all authors.

Notes

The authors declare no competing financial interest.

ACKNOWLEDGMENTS

This work was supported by the National Science Foundation (NSF) through the Northwestern Materials Research Science and Engineering Center under NSF Award no. DMR-1720139 and partly under NSF-DMR 1929356 (V.P.D. & RdR). We acknowledge the Army Research Office for a Multidisciplinary University Research Initiatives (MURI) award under grant number W911NF-15-1-0447. I.C. is supported by the NSF Graduate Research Fellowship under Grant no. (DGE-1842165). A.M.E. is supported by the NSF Research Fellowship under grant no. (DGE-1324585). This study made use of the EPIC facility of NUANCE Center at Northwestern University, which has received support from

the Soft and Hybrid Nanotechnology Experimental (SHyNE) Resource (NSF-ECCS 2025633), the MRSEC program (NSF DMR-1720139) at the Materials Research Center, the Keck Foundation, the State of Illinois, and International Institute for Nanotechnology (IIN). We acknowledge Gatan Inc., Pleasanton, CA, USA for the use of the K3-IS camera installed at the EPIC facility of Northwestern University's NUANCE Center. Research reported in this publication was supported in part by instrumentation provided by the Office of The Director, National Institutes of Health of the National Institutes of Health under Award Number S10OD026871. The content is solely the responsibility of the authors and does not necessarily represent the official views of the National Institutes of Health.

REFERENCES

- (1) Servalli, M.; Schlüter, A. D. Synthetic Two-Dimensional Polymers. *Annu. Rev. Mater. Res.* **2017**, 47, 361–389.
- (2) Colson, J. W.; Dichtel, W. R. Rationally Synthesized Two-Dimensional Polymers. *Nat. Chem.* **2013**, *5*, 453–465.
- (3) Segura, J. L.; Mancheño, M. J.; Zamora, F. Covalent Organic Frameworks Based on Schiff-Base Chemistry: Synthesis, Properties and Potential Applications. *Chem. Soc. Rev.* **2016**, *45*, 5635–5671.
- (4) Haase, F.; Troschke, E.; Savasci, G.; Banerjee, T.; Duppel, V.; Dörfler, S.; Grundei, M. M. J.; Burow, A. M.; Ochsenfeld, C.; Kaskel, S.; Lotsch, B. V. Topochemical Conversion of an Imine- into a Thiazole-Linked Covalent Organic Framework Enabling Real Structure Analysis. *Nat. Commun.* **2018**, *9*, 2600.
- (5) Wang, X.; Han, X.; Zhang, J.; Wu, X.; Liu, Y.; Cui, Y. Homochiral 2D Porous Covalent Organic Frameworks for Heterogeneous Asymmetric Catalysis. *J. Am. Chem. Soc.* **2016**, *138*, 12332–12335.
- (6) Lin, S.; Diercks, C. S.; Zhang, Y.-B.; Kornienko, N.; Nichols, E. M.; Zhao, Y.; Paris, A. R.; Kim, D.; Yang, P.; Yaghi, O. M.; Chang, C. J. Covalent organic frameworks comprising cobalt porphyrins for catalytic CO2reduction in water. *Science* **2015**, *349*, 1208–1213.
- (7) Xu, H.; Gao, J.; Jiang, D. Stable, Crystalline, Porous, Covalent Organic Frameworks as a Platform for Chiral Organocatalysts. *Nat. Chem.* **2015**, *7*, 905–912.
- (8) Valentino, L.; Matsumoto, M.; Dichtel, W. R.; Mariñas, B. J. Development and Performance Characterization of a Polyimine Covalent Organic Framework Thin-Film Composite Nanofiltration Membrane. *Environ. Sci. Technol.* **2017**, *51*, 14352–14359.
- (9) Corcos, A. R.; Levato, G. A.; Jiang, Z.; Evans, A. M.; Livingston, A. G.; Mariñas, B. J.; Dichtel, W. R. Reducing the Pore Size of Covalent Organic Frameworks in Thin-Film Composite Membranes Enhances Solute Rejection. *ACS Mater. Lett.* **2019**, *1*, 440–446.
- (10) Dey, K.; Pal, M.; Rout, K. C.; Kunjattu H, S.; Das, A.; Mukherjee, R.; Kharul, U. K.; Banerjee, R. Selective Molecular Separation by Interfacially Crystallized Covalent Organic Framework Thin Films. J. Am. Chem. Soc. 2017, 139, 13083–13091.
- (11) Chandra, S.; Kundu, T.; Kandambeth, S.; BabaRao, R.; Marathe, Y.; Kunjir, S. M.; Banerjee, R. Phosphoric Acid Loaded Azo (-N=N-) Based Covalent Organic Framework for Proton Conduction. *J. Am. Chem. Soc.* **2014**, *136*, 6570–6573.
- (12) Guo, J.; Xu, Y.; Jin, S.; Chen, L.; Kaji, T.; Honsho, Y.; Addicoat, M. A.; Kim, J.; Saeki, A.; Ihee, H.; Seki, S.; Irle, S.; Hiramoto, M.; Gao, J.; Jiang, D. Conjugated Organic Framework with Three-Dimensionally Ordered Stable Structure and Delocalized π Clouds. *Nat. Commun.* **2013**, *4*, 2736.
- (13) Jakowetz, A. C.; Hinrichsen, T. F.; Ascherl, L.; Sick, T.; Calik, M.; Auras, F.; Medina, D. D.; Friend, R. H.; Rao, A.; Bein, T. Excited-State Dynamics in Fully Conjugated 2D Covalent Organic Frameworks. J. Am. Chem. Soc. 2019, 141, 11565–11571.
- (14) Sick, T.; Hufnagel, A. G.; Kampmann, J.; Kondofersky, I.; Calik, M.; Rotter, J. M.; Evans, A.; Döblinger, M.; Herbert, S.; Peters, K.; Böhm, D.; Knochel, P.; Medina, D. D.; Fattakhova-Rohlfing, D.; Bein, T. Oriented Films of Conjugated 2D Covalent Organic Frameworks

- as Photocathodes for Water Splitting. J. Am. Chem. Soc. 2018, 140, 2085–2092.
- (15) Côté, A. P.; Benin, A. I.; Ockwig, N. W.; O'Keeffe, M.; Matzger, A. J.; Yaghi, O. M. Porous, Crystalline, Covalent Organic Frameworks. *Science* **2005**, *310*, 1166–1170.
- (16) Smith, B. J.; Dichtel, W. R. Mechanistic Studies of Two-Dimensional Covalent Organic Frameworks Rapidly Polymerized from Initially Homogenous Conditions. *J. Am. Chem. Soc.* **2014**, *136*, 8783–8789.
- (17) Matsumoto, M.; Valentino, L.; Stiehl, G. M.; Balch, H. B.; Corcos, A. R.; Wang, F.; Ralph, D. C.; Mariñas, B. J.; Dichtel, W. R. Lewis-Acid-Catalyzed Interfacial Polymerization of Covalent Organic Framework Films. *Chem* **2018**, *4*, 308–317.
- (18) Khayum, M. A.; Kandambeth, S.; Mitra, S.; Nair, S. B.; Das, A.; Nagane, S. S.; Mukherjee, R.; Banerjee, R. Chemically Delaminated Free-Standing Ultrathin Covalent Organic Nanosheets. *Angew. Chem., Int. Ed.* **2016**, *55*, 15604–15608.
- (19) Burke, D. W.; Sun, C.; Castano, I.; Flanders, N. C.; Evans, A. M.; Vitaku, E.; McLeod, D. C.; Lambeth, R. H.; Chen, L. X.; Gianneschi, N. C.; Dichtel, W. R. Acid Exfoliation of Imine-linked Covalent Organic Frameworks Enables Solution Processing into Crystalline Thin Films. *Angew. Chem., Int. Ed.* **2020**, *59*, 5165–5171.
- (20) Medina, D. D.; Werner, V.; Auras, F.; Tautz, R.; Dogru, M.; Schuster, J.; Linke, S.; Döblinger, M.; Feldmann, J.; Knochel, P.; Bein, T. Oriented Thin Films of a Benzodithiophene Covalent Organic Framework. *ACS Nano* **2014**, *8*, 4042–4052.
- (21) Colson, J. W.; Woll, A. R.; Mukherjee, A.; Levendorf, M. P.; Spitler, E. L.; Shields, V. B.; Spencer, M. G.; Park, J.; Dichtel, W. R. Oriented 2D Covalent Organic Framework Thin Films on Single-Layer Graphene. *Science* **2011**, 332, 228–231.
- (22) Zhao, Y.; Guo, L.; Gándara, F.; Ma, Y.; Liu, Z.; Zhu, C.; Lyu, H.; Trickett, C. A.; Kapustin, E. A.; Terasaki, O.; Yaghi, O. M. A Synthetic Route for Crystals of Woven Structures, Uniform Nanocrystals, and Thin Films of Imine Covalent Organic Frameworks. J. Am. Chem. Soc. 2017, 139, 13166–13172.
- (23) Smith, B. J.; Parent, L. R.; Overholts, A. C.; Beaucage, P. A.; Bisbey, R. P.; Chavez, A. D.; Hwang, N.; Park, C.; Evans, A. M.; Gianneschi, N. C.; Dichtel, W. R. Colloidal Covalent Organic Frameworks. *ACS Cent. Sci.* **2017**, *3*, 58–65.
- (24) Kim, K.; Lee, Z.; Regan, W.; Kisielowski, C.; Crommie, M. F.; Zettl, A. Grain Boundary Mapping in Polycrystalline Graphene. *ACS Nano* **2011**, *5*, 2142–2146.
- (25) Huang, P. Y.; Ruiz-Vargas, C. S.; van der Zande, A. M.; Whitney, W. S.; Levendorf, M. P.; Kevek, J. W.; Garg, S.; Alden, J. S.; Hustedt, C. J.; Zhu, Y.; Park, J.; McEuen, P. L.; Muller, D. A. Grains and Grain Boundaries in Single-Layer Graphene Atomic Patchwork Quilts. *Nature* **2011**, *469*, 389–392.
- (26) Ishihara, M.; Koga, Y.; Kim, J.; Tsugawa, K.; Hasegawa, M. Direct Evidence of Advantage of Cu(111) for Graphene Synthesis by Using Raman Mapping and Electron Backscatter Diffraction. *Mater. Lett.* **2011**, *65*, 2864–2867.
- (27) Britton, T. B.; Jiang, J.; Guo, Y.; Vilalta-Clemente, A.; Wallis, D.; Hansen, L. N.; Winkelmann, A.; Wilkinson, A. J. Tutorial: Crystal orientations and EBSD Or which way is up? *Mater. Charact.* **2016**, *117*, 113–126.
- (28) Panova, O.; Ophus, C.; Takacs, C. J.; Bustillo, K. C.; Balhorn, L.; Salleo, A.; Balsara, N.; Minor, A. M. Diffraction imaging of nanocrystalline structures in organic semiconductor molecular thin films. *Nat. Mater.* **2019**, *18*, 860–865.
- (29) Abbasi, K.; Wang, D.; Fusella, M. A.; Rand, B. P.; Avishai, A. Methods for Conducting Electron Backscattered Diffraction (EBSD) on Polycrystalline Organic Molecular Thin Films. *Microsc. Microanal.* **2018**, *24*, 420–423.
- (30) Trimby, P.; Bewick, A.; Abou-Ras, D.; Caprioglio, P.; Neher, D.; Otter, L. The Analysis of Sensitive Materials Using EBSD: The Importance of Beam Conditions and Detector Sensitivity. *Microsc. Microanal.* **2019**, *25*, 2394–2395.
- (31) Susi, T.; Kotakoski, J.; Arenal, R.; Kurasch, S.; Jiang, H.; Skakalova, V.; Stephan, O.; Krasheninnikov, A. V.; Kauppinen, E. I.;

- Kaiser, U.; Meyer, J. C. Atomistic Description of Electron Beam Damage in Nitrogen-Doped Graphene and Single-Walled Carbon Nanotubes. *ACS Nano* **2012**, *6*, 8837–8846.
- (32) Ugurlu, O.; Haus, J.; Gunawan, A. A.; Thomas, M. G.; Maheshwari, S.; Tsapatsis, M.; Mkhoyan, K. A. Radiolysis to Knockon Damage Transition in Zeolites under Electron Beam Irradiation. *Phys. Rev. B: Condens. Matter Mater. Phys.* **2011**, 83, 113408.
- (33) Garcia, A.; Raya, A. M.; Mariscal, M. M.; Esparza, R.; Herrera, M.; Molina, S. I.; Scavello, G.; Galindo, P. L.; Jose-Yacaman, M.; Ponce, A. Analysis of electron beam damage of exfoliated MoS2 sheets and quantitative HAADF-STEM imaging. *Ultramicroscopy* **2014**, *146*, 33–38.
- (34) Zhang, D.; Zhu, Y.; Liu, L.; Ying, X.; Hsiung, C.-E.; Sougrat, R.; Li, K.; Han, Y. Atomic-resolution transmission electron microscopy of electron beam-sensitive crystalline materials. *Science* **2018**, 359, 675–679.
- (35) Wang, W.; Schlüter, A. D. Synthetic 2D Polymers: A Critical Perspective and a Look into the Future. *Macromol. Rapid Commun.* **2019**, *40*, 1800719.
- (36) Evans, A. M.; Parent, L. R.; Flanders, N. C.; Bisbey, R. P.; Vitaku, E.; Kirschner, M. S.; Schaller, R. D.; Chen, L. X.; Gianneschi, N. C.; Dichtel, W. R. Seeded Growth of Single-Crystal Two-Dimensional Covalent Organic Frameworks. *Science* **2018**, *361*, 52–57.
- (37) Peng, Y.; Huang, Y.; Zhu, Y.; Chen, B.; Wang, L.; Lai, Z.; Zhang, Z.; Zhao, M.; Tan, C.; Yang, N.; Shao, F.; Han, Y.; Zhang, H. Ultrathin Two-Dimensional Covalent Organic Framework Nanosheets: Preparation and Application in Highly Sensitive and Selective DNA Detection. *J. Am. Chem. Soc.* **2017**, *139*, 8698–8704.
- (38) Ascherl, L.; Sick, T.; Margraf, J. T.; Lapidus, S. H.; Calik, M.; Hettstedt, C.; Karaghiosoff, K.; Döblinger, M.; Clark, T.; Chapman, K. W.; Auras, F.; Bein, T. Molecular Docking Sites Designed for the Generation of Highly Crystalline Covalent Organic Frameworks. *Nat. Chem.* **2016**, *8*, 310–316.
- (39) Ascherl, L.; Evans, E. W.; Hennemann, M.; Di Nuzzo, D.; Hufnagel, A. G.; Beetz, M.; Friend, R. H.; Clark, T.; Bein, T.; Auras, F. Solvatochromic Covalent Organic Frameworks. *Nat. Commun.* **2018**, 9, 3802.
- (40) Auras, F.; Ascherl, L.; Hakimioun, A. H.; Margraf, J. T.; Hanusch, F. C.; Reuter, S.; Bessinger, D.; Döblinger, M.; Hettstedt, C.; Karaghiosoff, K.; Herbert, S.; Knochel, P.; Clark, T.; Bein, T. Synchronized Offset Stacking: A Concept for Growing Large-Domain and Highly Crystalline 2D Covalent Organic Frameworks. *J. Am. Chem. Soc.* **2016**, *138*, 16703–16710.
- (41) Bessinger, D.; Ascherl, L.; Auras, F.; Bein, T. Spectrally Switchable Photodetection with Near-Infrared-Absorbing Covalent Organic Frameworks. *J. Am. Chem. Soc.* **2017**, *139*, 12035–12042.
- (42) Dogru, M.; Handloser, M.; Auras, F.; Kunz, T.; Medina, D.; Hartschuh, A.; Knochel, P.; Bein, T. A Photoconductive Thienothiophene-Based Covalent Organic Framework Showing Charge Transfer Towards Included Fullerene. *Angew. Chem., Int. Ed.* **2013**, *52*, 2920–2924.
- (43) Dogru, M.; Sonnauer, A.; Zimdars, S.; Döblinger, M.; Knochel, P.; Bein, T. Facile Synthesis of a Mesoporous Benzothiadiazole-COF Based on a Transesterification Process. *CrystEngComm* **2013**, *15*, 1500–1502.
- (44) Vyas, V. S.; Haase, F.; Stegbauer, L.; Savasci, G.; Podjaski, F.; Ochsenfeld, C.; Lotsch, B. V. A Tunable Azine Covalent Organic Framework Platform for Visible Light-Induced Hydrogen Generation. *Nat. Commun.* **2015**, *6*, 8508.
- (45) Vyas, V. S.; Vishwakarma, M.; Moudrakovski, I.; Haase, F.; Savasci, G.; Ochsenfeld, C.; Spatz, J. P.; Lotsch, B. V. Exploiting Noncovalent Interactions in an Imine-Based Covalent Organic Framework for Quercetin Delivery. *Adv. Mater.* **2016**, 28, 8749–8754.
- (46) Haase, F.; Gottschling, K.; Stegbauer, L.; Germann, L. S.; Gutzler, R.; Duppel, V.; Vyas, V. S.; Kern, K.; Dinnebier, R. E.; Lotsch, B. V. Tuning the Stacking Behaviour of a 2D Covalent Organic Framework through Non-Covalent Interactions. *Mater. Chem. Front.* 2017, 1, 1354–1361.

- (47) Feng, X.; Schlüter, A. D. Towards Macroscopic Crystalline 2D Polymers. *Angew. Chem., Int. Ed.* **2018**, *57*, 13748–13763.
- (48) Banerjee, T.; Haase, F.; Trenker, S.; Biswal, B. P.; Savasci, G.; Duppel, V.; Moudrakovski, I.; Ochsenfeld, C.; Lotsch, B. V. Sub-Stoichiometric 2D Covalent Organic Frameworks from Tri- and Tetratopic Linkers. *Nat. Commun.* **2019**, *10*, 3046.
- (49) Murthy, A. A.; Stanev, T. K.; dos Reis, R.; Hao, S.; Wolverton, C.; Stern, N. P.; Dravid, V. P. Direct Visualization of Electric-Field-Induced Structural Dynamics in Monolayer Transition Metal Dichalcogenides. *ACS Nano* **2020**, *14*, 1569–1576.
- (50) Jin, L.; Milazzo, A.-C.; Kleinfelder, S.; Li, S.; Leblanc, P.; Duttweiler, F.; Bouwer, J. C.; Peltier, S. T.; Ellisman, M. H.; Xuong, N.-H. Applications of Direct Detection Device in Transmission Electron Microscopy. *J. Struct. Biol.* **2008**, *161*, 352–358.
- (51) Li, X.; Mooney, P.; Zheng, S.; Booth, C. R.; Braunfeld, M. B.; Gubbens, S.; Agard, D. A.; Cheng, Y. Electron Counting and Beam-Induced Motion Correction Enable near-Atomic-Resolution Single-Particle Cryo-EM. *Nat. Methods* **2013**, *10*, 584–590.
- (52) Spitler, E. L.; Koo, B. T.; Novotney, J. L.; Colson, J. W.; Uribe-Romo, F. J.; Gutierrez, G. D.; Clancy, P.; Dichtel, W. R. A 2D Covalent Organic Framework with 4.7-Nm Pores and Insight into Its Interlayer Stacking. *J. Am. Chem. Soc.* **2011**, *133*, 19416–19421.
- (53) Wan, S.; Guo, J.; Kim, J.; Ihee, H.; Jiang, D. A Belt-Shaped, Blue Luminescent, and Semiconducting Covalent Organic Framework. *Angew. Chem., Int. Ed.* **2008**, *47*, 8826–8830.
- (54) Jany, B. R.; Janas, A.; Krok, F. Automatic Microscopic Image Analysis by Moving Window Local Fourier Transform and Machine Learning. *Micron* **2020**, *130*, 102800.